

# Electron cryo-microscopy structure of a human TRPM4 channel

Paige A. Winkler<sup>1\*</sup>, Yihe Huang<sup>1\*</sup>, Weinan Sun<sup>2\*</sup>, Juan Du<sup>1</sup> & Wei Lü<sup>1</sup>

**Ca<sup>2+</sup>-activated, non-selective (CAN) ion channels** sense increases of the intracellular Ca<sup>2+</sup> concentration, producing a flux of Na<sup>+</sup> and/or K<sup>+</sup> ions that depolarizes the cell, thus modulating cellular Ca<sup>2+</sup> entry. CAN channels are involved in cellular responses such as neuronal bursting activity and cardiac rhythm. Here we report the electron cryo-microscopy structure of the most widespread CAN channel, human TRPM4, bound to the agonist Ca<sup>2+</sup> and the modulator decavanadate. Four cytosolic C-terminal domains form an umbrella-like structure with a coiled-coil domain for the ‘pole’ and four helical ‘ribs’ spanning the N-terminal TRPM homology regions (MHRs), thus holding four subunits in a crown-like architecture. We observed two decavanadate-binding sites, one in the C-terminal domain and another in the intersubunit MHR interface. A glutamine in the selectivity filter may be an important determinant of monovalent selectivity. Our structure provides new insights into the function and pharmacology of both the CAN and the TRPM families.

TRPM4 is a Ca<sup>2+</sup>-activated, non-selective cation channel that is permeable to monovalent sodium and potassium<sup>1–5</sup>. It is one of the eight members of the TRPM (melastatin-like transient receptor potential) subfamily of TRP channels<sup>6,7</sup>. TRPM family members are characteristically assembled with N-terminal TRPM homology regions (MHRs) and a C-terminal coiled-coil domain<sup>8–10</sup>. Widely expressed throughout the brain, heart, kidney, colon, and intestine, TRPM4 is directly involved in many biological processes, including cellular depolarization, cardiac rhythm generation, and the immune response<sup>11–14</sup>. Mutations in TRPM4 are associated with cardiac arrhythmias and dysfunctions, including Brugada syndrome<sup>15–17</sup>.

A unique property of TRPM4 and its closest homologue TRPM5 is that they are the only two members impermeable to Ca<sup>2+</sup> in the TRP superfamily<sup>18,19</sup>. However, the underlying molecular basis of this phenomenon remains elusive owing to the lack of knowledge of their selectivity filters. The hallmark MHR domain distinguishes TRPM from other TRP subfamilies, yet an atomic view of the MHR domain is missing. Unlike classic voltage-gated ion channels, the fourth transmembrane helix (S4) in TRPM4 only contains one positively charged residue. Nevertheless, TRPM4 displays weak voltage dependence<sup>1,20</sup>. Compounds such as decavanadate (DVT), a highly negatively charged metal cluster, shift the voltage dependence of TRPM4 towards negative potential<sup>21–23</sup>, but the underlying mechanism and the exact binding site of DVT remained unknown.

Here we present the structure of a full-length human TRPM4 bound with the agonist Ca<sup>2+</sup> and the modulator DVT at an overall resolution of 3.8 Å using single-particle electron cryo-microscopy (cryo-EM), revealing the unique architecture and domain arrangement in the TRPM family and providing a structural basis for DVT modulation and monovalent selectivity on TRPM4.

## Structure determination and overall architecture

The density map of TRPM4 was of sufficient quality to allow *de novo* building of the majority of the protein (Extended Data Figs 1–3). Densities for DVT were found in two different sites on each subunit: the first (DVT1) buried at the kink of the C-terminal helix and the

second (DVT2) exposed at the interface of the MHR domain between two adjacent subunits (Extended Data Fig. 4). Although the density for Ca<sup>2+</sup> was not discernible, our patch-clamp recording data showed Ca<sup>2+</sup> activation that can be blocked by flufenamic acid and ATP<sup>4–</sup> (Extended Data Fig. 5a–c).

Viewed parallel to the membrane, TRPM4 has an inverted crown-like shape, consisting of a transmembrane domain (TMD) and a large cytosolic domain formed by the N-terminal MHR domain and the C-terminal domain (CTD) (Fig. 1 and Extended Data Fig. 6). The four large MHR domains compose four peaks of the inverted crown (Fig. 1a). This entire construction is supported by four CTDs in an umbrella-like shape, in which four helical ‘ribs’ and a coiled-coil ‘pole’ span into MHR domains horizontally and vertically, respectively (Fig. 1b). Together, the MHR domain and the helical CTD of TRPM4 constitute a unique intracellular architecture that is distinct from that of any other TRP channels, in which the N-terminal cytosolic domains mainly consist of ankyrin repeats<sup>24–28</sup>.

## MHR domain

The MHR domain was divided into four homology regions (MHR1–MHR4) based on sequence similarity within the TRPM family<sup>8</sup>. Inspection of the structure, however, revealed that MHR1 and MHR2 form an intact domain structure, here termed MHR1/2. The entire MHR has an elongated shape stretching throughout the cytosolic domain, with MHR3 bridging between MHR1/2 and MHR4 (Figs 1d–f, 2a).

MHR1/2, residing underneath the CTD rib helix and distal to the TMD, possesses a complex topology consisting of a β-sheet core surrounded by α helices and loops (Figs 1d, 2a). MHR1/2 not only has extensive interaction with MHR3 within the same subunit (Fig. 2b), but also has weak contact with the MHR3 in the adjacent subunit, creating a binding pocket for DVT2 (Figs 1b, c, e, f, 2c), suggesting a role for the MHR in the sensing of external stimuli. In the β-sheet core, a highly conserved serine (S120) forms a polar interaction with the highly conserved E254 in a neighbouring α helix (Fig. 2b). Replacement of this serine by leucine in TRPM6 is reported to cause

<sup>1</sup>Van Andel Institute, 333 Bostwick Avenue N.E., Grand Rapids, Michigan 49503, USA. <sup>2</sup>Janelia Research Campus, 19700 Helix Drive, Ashburn, Virginia 20147, USA.  
\*These authors contributed equally to this work.

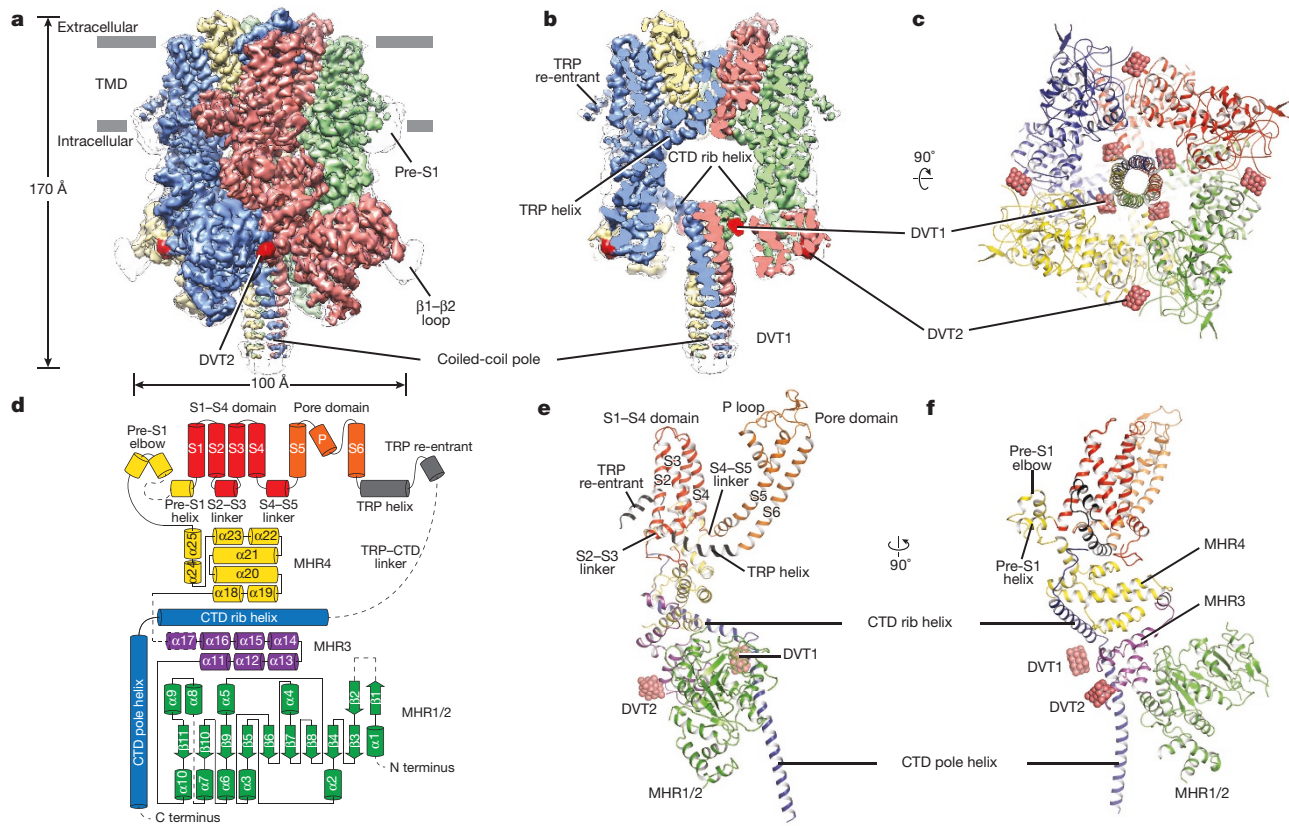


**Figure 1 | Overall architecture.** **a**, The three-dimensional reconstruction viewed parallel to the membrane, with four subunits in different colours. The DVT densities are red. The unsharpened reconstruction is shown as a transparent envelope. **b**, Slice view of the reconstruction. **c**, The

atomic model viewed from the cytosolic side. **d**, Domain organization. Dashed lines and cylinders denote regions that have not been modelled. **e**, **f**, Cartoon representation of one subunit colour-coded to match the diagram in **d**.

hereditary hypomagnesaemia by disrupting channel tetramerization<sup>29</sup>, suggesting a properly folded MHR1/2 is essential for channel assembly.

MHR4 is the domain proximal to the TMD and is positioned between the TMD and MHR3 (Fig. 2a). This domain shares surprising structural similarities to the domain in NOMPC (a mechanotransduction channel from *Drosophila*) that connects the ankyrin repeats and the TMD, particularly at the lower part, although they share low sequence similarity and a distinct overall architecture of an intracellular domain<sup>28</sup>. Therefore, we chose to consider the upper and lower parts of MHR4 and to compare them with NOMPC (Fig. 2a, d, e). The lower portion of MHR4, sharing the most structural similarity with NOMPC, interacts with the TRP domain and the S2-S3 linker of TMD on the top and with the rib helix of CTD and MHR3 on the bottom, suggesting a role in mediating the communication between the MHR, CTD, and TMD (Fig. 2a, d). The upper portion of MHR4, in contrast, differs remarkably between TRPM4 and NOMPC. First, in TRPM4 it is nearly threefold longer in amino acid sequence than in NOMPC (Fig. 2d, e and Extended Data Fig. 7). As a result, in addition to the pre-S1' elbow observed in NOMPC, it also has a short pre-S1 helix and a less well-defined structure connecting the pre-S1 helix and pre-S1 elbow. Second, the presence of the pre-S1 helix leads to a rotation of the pre-S1 elbow almost 90° towards the TMD in the adjacent subunit (Fig. 2e).

### C-terminal domain

The most notable feature of the TRPM4 structure is the umbrella-like CTD, in which approximately 90 residues of each subunit form an obtuse L shape. There is a break one-third of the way along the helical structure, thus dividing it into a horizontal and a vertical helix with a turn of approximately 120°, where a DVT molecule is found (Fig. 1e, f).

The CTD is rich in positively charged residues, particularly at the turn, creating a highly favourable environment for binding of negatively charged small molecules.

The vertical helices of the four subunits wind into the tetrameric coiled-coil pole assembly (Fig. 3a, b), one of the common features used to specify subunit assembly and assembly specificity within the voltage-gated ion channel superfamily<sup>27,30</sup>. Indeed, the truncation of the C-terminal coiled-coil domain hinders TRPM4 in forming a tetramer<sup>31</sup>. Those four helices run in the same direction, forming a parallel coiled-coil domain. This is consistent with the prediction that a parallel coiled-coil domain exists in TRPM2, TRPM4, TRPM5, and TRPM8, whereas TRPM1, TRPM3, TRPM6, and TRPM7 possess antiparallel coiled-coil domains<sup>32</sup>.

The horizontal rib helix is a new feature with elusive function (Fig. 3a, b). It penetrates through a large tunnel formed by neighbouring MHR domains and has multiple hydrophobic and polar contacts with the MHR, suggesting a possible contribution to channel assembly by the tethering together of the MHR domains (Fig. 3c, d). The rib helix further connects to the TRP domain through a flexible linker, and interestingly, these two domains are running in parallel when viewed perpendicular to the membrane (Fig. 3a, b). We speculate that these two domains may form a complicated communication network by which signals from the CTD and MHR can be transduced along the rib helix to the TRP domain, and ultimately to the gating helix S6 in the TMD to modulate ion channel activities.

Taken together, these findings indicate that the CTD may not only direct tetrameric assembly and assembly specificity, but also have an essential role in sensing ligands and modulating channel function through its connection to the TRP domain.

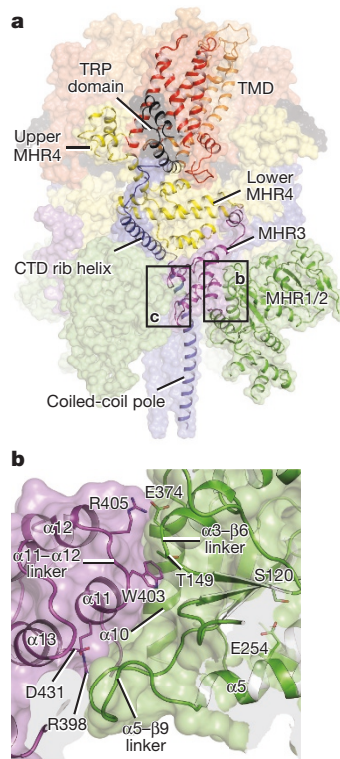


**Figure 2 | The MHR.** **a**, Domain organization. Colours match those in Fig. 1d. The intra-subunit and inter-subunit MHR1/2–MHR3 interfaces detailed in **b** and **c** are outlined in black. **b**, The intra-subunit interface is formed by the  $\alpha_3$ – $\beta_6$  and  $\alpha_5$ – $\beta_9$  linkers, and  $\alpha_{10}$  in MHR1/2, and the  $\alpha_{11}$ – $\alpha_{12}$  linker and  $\alpha_{13}$  in MHR3. **c**, The inter-subunit interface is formed by the  $\beta_3$ – $\beta_4$  and  $\beta_7$ – $\beta_8$  linkers in MHR1/2, and the  $\alpha_{14}$ – $\alpha_{15}$  linker in the adjacent MHR3. **d**, Superposition of the TRPM4 (residues 1136–1262) and NOMPC (grey, residues 1263–1297) using the  $C_\alpha$  of lower MHR4. Only the MHR4, TMD and TRP domain are shown. **e**, Differences between upper MHR4 in TRPM4 (wheat) and NOMPC (grey).

### DVT-binding sites

DVT modulates the voltage dependence of TRPM4<sup>21</sup> (Extended Data Fig. 5d–l). Moreover, we found that DVT modulates  $\text{Ca}^{2+}$ -activated current amplitude in a  $\text{Ca}^{2+}$ -concentration-dependent manner (Extended Data Fig. 5d–l). We identified two DVT-binding sites, both of which possess a high density of positively charged residues, providing an ideal place for DVT (Fig. 4a, b). The first binding site is at the turning point of the coiled-coil pole and helical rib of the CTD, consistent with previous predictions<sup>21</sup>. There, the DVT1 molecule is docked into a pocket formed by six positively charged residues, along with some other polar and acidic residues (Fig. 4a). Deletion of a six-amino-acid segment containing one of the six positively charged residues, Arg1141, completely abolished the DVT modulation effect<sup>21</sup>. The second binding site is in the interface between MHR1/2 and MHR3 from the adjacent subunit, where three positively charged arginine residues are found (Fig. 4b). Despite being the closest homologue of TRPM4, TRPM5 is insensitive to DVT. Sequence alignment reveals that one of the key residues in the DVT1 site, Arg1147, as well as all the three positively charged residues in DVT2 site, are not conserved in TRPM5 (Extended Data Fig. 7), explaining its insensitivity to DVT.

### TRP domain

Bridging between the CTD rib helix and the gating helix S6, the TRP domain is considered a key determinant for signal transduction and channel gating<sup>33–36</sup>. The TRP domain is not a continuous  $\alpha$  helix but rather has a break at about two-thirds of the helical structure length, thus dividing the TRP domain into two segments. The first segment is the helical stretch running parallel to the cytosolic surface of the

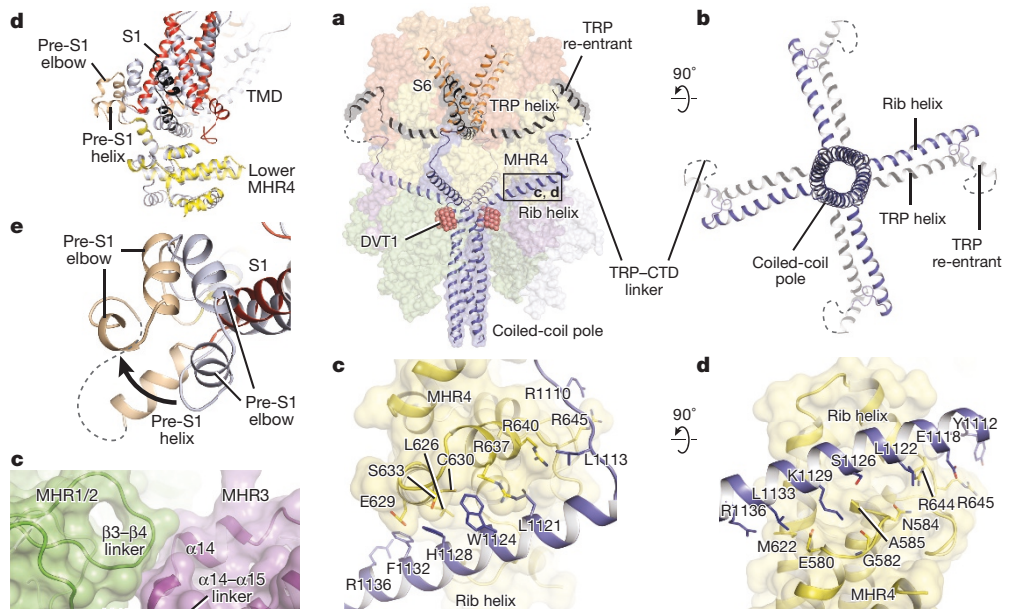


**Figure 3 | The CTD.** **a**, Cartoon representation of the CTD, the TRP helix and TRP re-entrant, and S6. Disordered TRP–CTD linkers are shown as dashed lines. The colour codes match those in Fig. 1d. For clarity, MHR1–3 of the front right subunit is greyed out. The interaction of the CTD rib helix with MHR4 detailed in **c** and **d** is outlined in black. **b**, The CTD and TRP domains viewed from the cytosolic side. **c**, **d**, Interaction between the CTD rib helix and MHR4.

membrane as an extension of S6, termed the TRP helix. The second segment connecting to the CTD rib helix is a re-entrant loop and helix, half of which is embedded in the membrane between S1 and S2 as a short loop and the other half returns to the cytoplasmic side as a helix termed the TRP re-entrant (Fig. 3a).

TRPM4 exhibits weak voltage-dependency. In contrast to classical voltage-gated potassium channels, only 1 of the 3–5 positively charged residues in S4 that contribute to gating charge is conserved in TRPM4 (Arg905), which corresponds most closely to R4 in Kv1.2–Kv2.1 paddle chimaera (Kvchim)<sup>37</sup>. Moreover, TRPM4 and its related proteins TRPM2, TRPM5 and TRPM8 all contain two basic residues (Lys914 and Lys919 in TRPM4) in the S4–S5 linker (Extended Data Figs 7, 8). Charge-neutralizing mutations of these three positively charged residues in TRPM8 shift the voltage dependence, suggesting that both S4 and the S4–S5 linker are important for voltage sensing in these channels<sup>38</sup>. The TRP helix forms extensive interactions with the S4–S5 linker and S1 on the top and with MHR4 on the bottom, suggesting a number of mechanisms by which activities of the voltage sensor domain

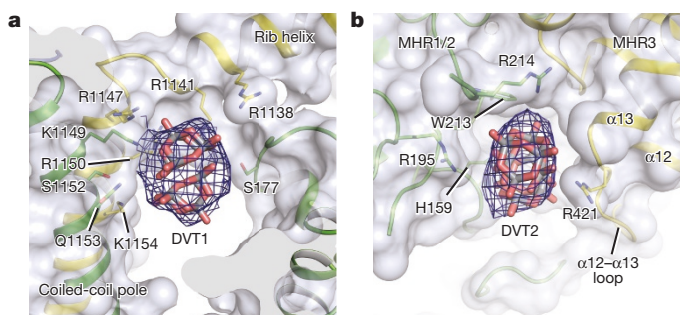


**Figure 4 | DVT-binding sites.** **a**, DVT1 binds at the junction of the CTD pole and the rib helix. **b**, DVT2 binds at the interface of MHR1/2 (green) and the MHR3 (yellow) from the adjacent subunit. **a**, **b**, Residues that interact with DVT are shown as sticks, DVT densities are shown in mesh.

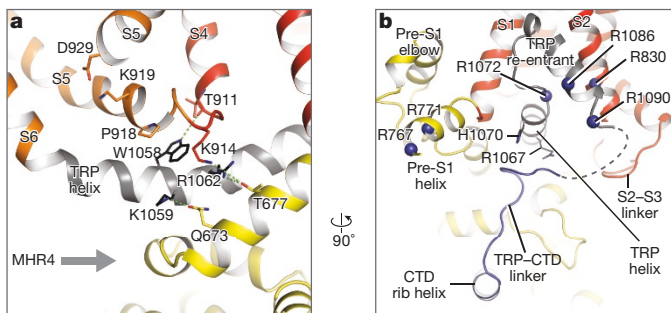


**Figure 5 | TRP domain.** **a**, Cartoon representation of the TRP helix (grey), transmembrane helices (red and orange), and MHR4 (yellow). **b**, Interaction of the TRP re-entrant (grey) with the transmembrane helices (red) and the TRP-CTD linker (blue). MHR4 is yellow. Positively charged residues within and near the TRP re-entrant are shown as blue spheres. Residues in the TRP helix in close contact with the TRP-CTD linker are shown as sticks.

S1–S4 (including the S4–S5 linker) or the MHR can affect the TRP helix, ultimately modulating channel gating (Fig. 5). Specifically, the invariant residue Trp1058 on the TRP helix is embraced by the S4–S5 linker, probably stacking with the highly conserved Pro918 and forming a possible hydrogen bond with the main-chain carbonyl oxygen of Thr911, suggesting a possible coupling mechanism between membrane potential and channel gating (Fig. 5a). Mutation of this tryptophan in TRPV3 results in Olmsted syndrome and replacement of the same residue in NOMPC results in a channel with increased current amplitude but that is nonresponsive to mechanical stimuli<sup>28,39</sup>.

The TRP re-entrant harbours three positively charged arginine residues (Arg1072, Arg1086, and Arg1090) (Fig. 5b), providing an ideal binding site for membrane-bound phosphatidylinositol-4,5-bisphosphate (PtdIns(4,5)P<sub>2</sub>). Whereas neutralization of Arg1072 in TRPM4 did not affect PtdIns(4,5)P<sub>2</sub> sensitivity, neutralization of the equivalent residue in TRPM8 did<sup>22,40</sup>. Furthermore, the communication of the TRP domain with the CTD is not only through direct connection between the TRP re-entrant and the CTD rib helix through a partially disordered linker, but also through the close contact between the tip of this linker and the TRP helix (Fig. 5b). These connections provide a possible mechanism by which the ligands bound to the CTD, such as DVT, modulate channel gating by transducing the signal through the TRP domain.

### Ion-conducting pore

Like other voltage-gated ion channels<sup>24,37,41,42</sup>, TRPM4 has two restriction sites, a selectivity filter formed by the P loop close to the extracellular side and a gate shaped by S6 close to the intracellular side (Fig. 6a, b). The selectivity filter has the smallest radius, 2.1 Å, restricted by the main-chain carbonyls of F975 and G976 and the side chain of Q977. This size is similar to the size observed in NOMPC and TRPV1 in the open state, allowing permeation of partially hydrated cations. By contrast, the narrowest constriction of the intracellular gate has a radius of 0.8 Å that is defined by the side chains of I1040 and S1044; that radius is too small to conduct ions. We thus suggest that the structure represents an agonist- and modulator-bound closed state.

TRPM4 and TRPM5 are the only two members of the TRP family impermeable to Ca<sup>2+</sup>. In TRPM4 we noted a neutral glutamine (Q977) that is equivalent to Q920 in human TRPM5 forms part of the selectivity filter, whereas in most Ca<sup>2+</sup>-permeable TRP channels there is an acidic residue (Fig. 6c and Extended Data Fig. 9). Replacement of the glutamine by an acidic residue results in moderate Ca<sup>2+</sup> permeability<sup>43</sup>. However, neutralization of the corresponding acidic residue in TRPV1 markedly decreases its permeability for divalent cations<sup>44</sup>. Therefore, an acidic amino acid at this position is probably an important molecular determinant for Ca<sup>2+</sup> permeability, perhaps by creating a Ca<sup>2+</sup> binding site<sup>45</sup>. Interestingly, TRPM2 and TRPM8, both of which are permeable

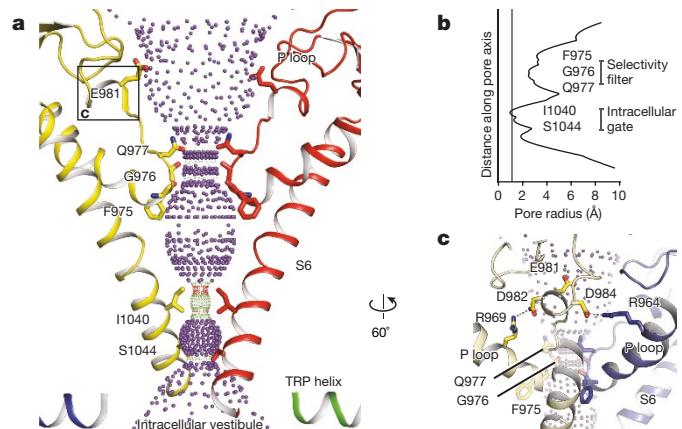


**Figure 6 | Ion-conducting pore.** **a**, The shape and size of the ion-conducting pore. The P loop and S6 of two subunits and the TRP helix of the other two subunits are shown in cartoon representation and the side chains of restriction residues are shown as sticks. The region outlined in black contains the acidic <sup>981</sup>Glu-Asp-Met-Glu sequence and is expanded in **c**. Purple, green, and red spheres define radii of >2.3, 1.2–2.3, and <1.2 Å, respectively. **b**, Plot of pore radius as a function of distance along the pore axis. **c**, The acidic <sup>981</sup>Glu-Asp-Met-Glu sequence and its interaction with residues within the same unit (yellow) and in an adjacent subunit (blue).

to Ca<sup>2+</sup>, also have a glutamine residue at this position. However, their P loops are one residue shorter than that of TRPM4 and TRPM5, which perhaps results in a different selectivity filter configuration<sup>43</sup>.

An acidic sequence of <sup>981</sup>Glu-Asp-Met-Glu is located at the extracellular side of the selectivity filter, and Glu981 is the only charged residue facing the ion-conducting pore (Fig. 6c). Neutralization of Glu981 is reported to strongly reduce intracellular spermine blockage<sup>43</sup>. The other two acidic residues, Asp982 and Asp984, interact with positively charged residues either within the same subunit or in the adjacent subunit, and they may play an important role in maintaining the pore structure. Indeed, neutralization of Asp982 markedly increased the desensitization rate, and neutralization of Asp984 resulted in loss of function<sup>43</sup>.

### Conclusion

The TRPM4 structure has an inverted crown-like cytosolic architecture with large N-terminal MHR domains composing the four peaks of the crown. The CTDs form an umbrella-like structure with a coiled-coil domain as the pole and four horizontal helical ribs stretching through the MHR domains and thus sustaining the entire channel architecture. Two modulator DVT-binding sites are located at the turn of the CTD and at the interface between MHR1/2 and the adjacent MHR3, suggesting that DVT can exert its modulation effect on channel gating through both the CTD and the N-terminal MHR. Moreover, a glutamine in the selectivity filter may hinder TRPM4 permeability to Ca<sup>2+</sup>. Our structural work on TRPM4 provides an atomic view of the TRPM family channels and also a molecular framework for understanding channel function and for developing new therapeutics.

**Online Content** Methods, along with any additional Extended Data display items and Source Data, are available in the online version of the paper; references unique to these sections appear only in the online paper.

**Received 4 August; accepted 23 October 2017.**

**Published online 6 December 2017.**

1. Nilius, B. et al. Voltage dependence of the Ca<sup>2+</sup>-activated cation channel TRPM4. *J. Biol. Chem.* **278**, 30813–30820 (2003).
2. Launay, P. et al. TRPM4 is a Ca<sup>2+</sup>-activated nonselective cation channel mediating cell membrane depolarization. *Cell* **109**, 397–407 (2002).
3. Cléménçon, B. et al. Expression, purification, and projection structure by single particle electron microscopy of functional human TRPM4 heterologously expressed in *Xenopus laevis* oocytes. *Protein Expr. Purif.* **95**, 169–176 (2014).

4. Constantine, M. et al. Heterologously-expressed and liposome-reconstituted human transient receptor potential melastatin 4 channel (TRPM4) is a functional tetramer. *Sci. Rep.* **6**, 19352 (2016).
5. Guinamard, R., Demion, M., Magaud, C., Potreau, D. & Bois, P. Functional expression of the TRPM4 cationic current in ventricular cardiomyocytes from spontaneously hypertensive rats. *Hypertension* **48**, 587–594 (2006).
6. Harteneck, C. Function and pharmacology of TRPM cation channels. *Nauyn Schmiedebergs Arch. Pharmacol.* **371**, 307–314 (2005).
7. Kraft, R. & Harteneck, C. The mammalian melastatin-related transient receptor potential cation channels: an overview. *Pflugers Arch.* **451**, 204–211 (2005).
8. Clapham, D. E. TRP channels as cellular sensors. *Nature* **426**, 517–524 (2003).
9. Fleig, A. & Penner, R. The TRPM ion channel subfamily: molecular, biophysical and functional features. *Trends Pharmacol. Sci.* **25**, 633–639 (2004).
10. Perraud, A. L., Schmitz, C. & Scharenberg, A. M. TRPM2  $\text{Ca}^{2+}$  permeable cation channels: from gene to biological function. *Cell Calcium* **33**, 519–531 (2003).
11. Guinamard, R., Chatelier, A., Lenfant, J. & Bois, P. Activation of the  $\text{Ca}^{2+}$ -activated nonselective cation channel by diacylglycerol analogues in rat cardiomyocytes. *J. Cardiovasc. Electrophysiol.* **15**, 342–348 (2004).
12. Earley, S., Waldron, B. J. & Brayden, J. E. Critical role for transient receptor potential channel TRPM4 in myogenic constriction of cerebral arteries. *Circ. Res.* **95**, 922–929 (2004).
13. Gonzales, A. L., Garcia, Z. I., Amberg, G. C. & Earley, S. Pharmacological inhibition of TRPM4 hyperpolarizes vascular smooth muscle. *Am. J. Physiol. Cell Physiol.* **299**, C1195–C1202 (2010).
14. Barbet, G. et al. The calcium-activated nonselective cation channel TRPM4 is essential for the migration but not the maturation of dendritic cells. *Nat. Immunol.* **9**, 1148–1156 (2008).
15. Stallmeyer, B. et al. Mutational spectrum in the  $\text{Ca}^{2+}$ -activated cation channel gene TRPM4 in patients with cardiac conductance disturbances. *Hum. Mutat.* **33**, 109–117 (2012).
16. Liu, H. et al. Molecular genetics and functional anomalies in a series of 248 Brugada cases with 11 mutations in the TRPM4 channel. *PLoS ONE* **8**, e54131 (2013).
17. Demion, M. et al. Trpm4 gene invalidation leads to cardiac hypertrophy and electrophysiological alterations. *PLoS ONE* **9**, e115256 (2014).
18. Hof, T. et al. TRPM4 non-selective cation channels influence action potentials in rabbit Purkinje fibres. *J. Physiol. (Lond.)* **594**, 295–306 (2016).
19. Ullrich, N. D. et al. Comparison of functional properties of the  $\text{Ca}^{2+}$ -activated cation channels TRPM4 and TRPM5 from mice. *Cell Calcium* **37**, 267–278 (2005).
20. Hofmann, T., Chubanov, V., Gudermann, T. & Montell, C. TRPM5 is a voltage-modulated and  $\text{Ca}^{2+}$ -activated monovalent selective cation channel. *Curr. Biol.* **13**, 1153–1158 (2003).
21. Nilius, B., Prenen, J., Janssens, A., Voets, T. & Droogmans, G. Decavanadate modulates gating of TRPM4 cation channels. *J. Physiol. (Lond.)* **560**, 753–765 (2004).
22. Nilius, B. et al. The  $\text{Ca}^{2+}$ -activated cation channel TRPM4 is regulated by phosphatidylinositol 4,5-biphosphate. *EMBO J.* **25**, 467–478 (2006).
23. Zhang, Z., Okawa, H., Wang, Y. & Liman, E. R. Phosphatidylinositol 4,5-bisphosphate rescues TRPM4 channels from desensitization. *J. Biol. Chem.* **280**, 39185–39192 (2005).
24. Liao, M., Cao, E., Julius, D. & Cheng, Y. Structure of the TRPV1 ion channel determined by electron cryo-microscopy. *Nature* **504**, 107–112 (2013).
25. Cao, E., Liao, M., Cheng, Y. & Julius, D. TRPV1 structures in distinct conformations reveal activation mechanisms. *Nature* **504**, 113–118 (2013).
26. Shen, P. S. et al. The structure of the polycystic kidney disease channel PKD2 in lipid nanodiscs. *Cell* **167**, 763–773 (2016).
27. Paulsen, C. E., Armache, J. P., Gao, Y., Cheng, Y. & Julius, D. Structure of the TRPA1 ion channel suggests regulatory mechanisms. *Nature* **520**, 511–517 (2015).
28. Jin, P. et al. Electron cryo-microscopy structure of the mechanotransduction channel NOMPC. *Nature* **547**, 118–122 (2017).
29. Chubanov, V. et al. Disruption of TRPM6/TRPM7 complex formation by a mutation in the TRPM6 gene causes hypomagnesemia with secondary hypocalcemia. *Proc. Natl. Acad. Sci. USA* **101**, 2894–2899 (2004).
30. Sun, J. & MacKinnon, R. Cryo-EM structure of a KCNQ1/CaM complex reveals insights into congenital long QT syndrome. *Cell* **169**, 1042–1050 (2017).
31. Launay, P. et al. TRPM4 regulates calcium oscillations after T cell activation. *Science* **306**, 1374–1377 (2004).
32. Fujiwara, Y. & Minor, D. L. Jr. X-ray crystal structure of a TRPM assembly domain reveals an antiparallel four-stranded coiled-coil. *J. Mol. Biol.* **383**, 854–870 (2008).
33. Gregorio-Teruel, L. et al. The integrity of the TRP domain is pivotal for correct TRPV1 channel gating. *Biophys. J.* **109**, 529–541 (2015).
34. García-Sanz, N. et al. A role of the transient receptor potential domain of vanilloid receptor I in channel gating. *J. Neurosci.* **27**, 11641–11650 (2007).
35. Gregorio-Teruel, L., Valente, P., González-Ros, J. M., Fernández-Ballester, G. & Ferrer-Montiel, A. Mutation of I696 and W697 in the TRP box of vanilloid receptor subtype I modulates allosteric channel activation. *J. Gen. Physiol.* **143**, 361–375 (2014).
36. Valente, P. et al. Identification of molecular determinants of channel gating in the transient receptor potential box of vanilloid receptor I. *FASEB J.* **22**, 3298–3309 (2008).
37. Long, S. B., Tao, X., Campbell, E. B. & MacKinnon, R. Atomic structure of a voltage-dependent  $\text{K}^+$  channel in a lipid membrane-like environment. *Nature* **450**, 376–382 (2007).
38. Voets, T., Owsianik, G., Janssens, A., Talavera, K. & Nilius, B. TRPM8 voltage sensor mutants reveal a mechanism for integrating thermal and chemical stimuli. *Nat. Chem. Biol.* **3**, 174–182 (2007).
39. Lin, Z. et al. Exome sequencing reveals mutations in TRPV3 as a cause of Olmsted syndrome. *Am. J. Hum. Genet.* **90**, 558–564 (2012).
40. Rohács, T., Lopes, C. M., Michailidis, I. & Logothetis, D. E. P(4,5)P2 regulates the activation and desensitization of TRPM8 channels through the TRP domain. *Nat. Neurosci.* **8**, 626–634 (2005).
41. Ahuja, S. et al. Structural basis of Nav1.7 inhibition by an isoform-selective small-molecule antagonist. *Science* **350**, aac5464 (2015).
42. Wu, J. et al. Structure of the voltage-gated calcium channel  $\text{Ca}_{v}1.1$  at 3.6 Å resolution. *Nature* **537**, 191–196 (2016).
43. Nilius, B. et al. The selectivity filter of the cation channel TRPM4. *J. Biol. Chem.* **280**, 22899–22906 (2005).
44. García-Martínez, C., Morenilla-Palao, C., Planells-Cases, R., Merino, J. M. & Ferrer-Montiel, A. Identification of an aspartic residue in the P-loop of the vanilloid receptor that modulates pore properties. *J. Biol. Chem.* **275**, 32552–32558 (2000).
45. Tang, L. et al. Structural basis for  $\text{Ca}^{2+}$  selectivity of a voltage-gated calcium channel. *Nature* **505**, 56–61 (2014).

**Supplementary Information** is available in the online version of the paper.

**Acknowledgements** Cryo-EM data was collected at the David Van Andel Advanced Cryo-Electron Microscopy Suite in the Van Andel Research Institute (VARI) and we are grateful to G. Zhao and X. Meng for technical support. We thank C. Xu for help with SerialEM, the HPC team at VARI for computational support and D. Nadziejka for proofreading. This work is supported by internal funding from VARI.

**Author Contributions** W.L. designed the project. P.A.W., Y.H. and W.L. purified TRPM4 and performed cryo-EM data collection and processing. W.S. performed electrophysiological experiments. W.L. and J.D. analysed the data and wrote the manuscript. All the authors contributed in preparing the manuscript.

**Author Information** Reprints and permissions information is available at [www.nature.com/reprints](http://www.nature.com/reprints). The authors declare no competing financial interests. Readers are welcome to comment on the online version of the paper. Publisher's note: Springer Nature remains neutral with regard to jurisdictional claims in published maps and institutional affiliations. Correspondence and requests for materials should be addressed to W.L. (wei.lu@vai.org).

## METHODS

**TRPM4 expression and purification.** The gene encoding human full-length TRPM4 (UniProtKB (<http://www.uniprot.org>) accession number, Q8TD43) was synthesized by Bio Basic and was sub-cloned into pEG BacMam vector with a His tag, GFP, and a thrombin cleavage site at the N terminus<sup>46</sup>. Bacmid and baculovirus of TRPM4 in a BacMam vector were generated, and P2 viruses were used to infect a suspension of HEK293 GnT<sup>-</sup> cells. Cells were incubated at 37 °C for 12 h. Subsequently, 10 mM sodium butyrate was added to the culture and the temperature was set to 30 °C. The cells were collected 72 h post-infection, resuspended in a buffer containing 150 mM NaCl and 20 mM Tris 8.0 (TBS buffer) in the presence of 1 mM PMSF, 0.8 μM aprotinin, 2 μg ml<sup>-1</sup> leupeptin, and 2 mM pepstatin A (protease inhibitors), and subsequently lysed by sonication for 15 min. The membrane fraction was collected by centrifugation at 186,000g using 45 Ti rotor (Beckman Coulter, Inc.) for 1 h at 4 °C. It was then homogenized with a Dounce homogenizer in TBS buffer supplemented with protease inhibitors. The protein was extracted from membrane fraction with TBS buffer supplemented with 1% MNG-3, protease inhibitors, and 2 mM cholestryl hemisuccinate (CHS) for 1 h at 4 °C. The solubilized proteins were incubated with TALON resin and after washing with TBS buffer supplemented with 1 mM MNG-3, 0.2 mM CHS, and 10 mM imidazole, the bound TRPM4 was eluted with the same buffer, supplemented with 250 mM imidazole. The proteins were concentrated and further purified by size-exclusion chromatography in TBS buffer containing 1 mM N-dodecyl β-D-maltoside (DDM) and 0.2 mM CHS. Peak fractions containing the channel were pooled and concentrated to 4 mg ml<sup>-1</sup>.

**EM sample preparation and data acquisition.** A solution in which DVT is the primary molecular species was obtained by making a 50 mM solution of sodium orthovanadate (Na<sub>3</sub>VO<sub>4</sub>) in water and adjusting the pH to 2.0<sup>47,48</sup>. The solution was used within 6 h of preparation. Purified TRPM4 was mixed with 5 mM calcium chloride and 1 mM DVT a few hours before grid preparation. Blotting of a 2.5 μl sample at a concentration of 4 mg ml<sup>-1</sup> was applied to a glow-discharged Quantifoil holey carbon grid (gold, 1.2/1.3 μm size/hole space, 300 mesh), blotted using a Vitrobot Mark III using 2.5 s blotting time with 100% humidity, and then plunge-frozen in liquid ethane cooled by liquid nitrogen. Images were taken by an FEI Titan Krios electron microscope operating at 300 kV with a nominal magnification of 130,000×. Images were recorded by a Gatan K2 Summit direct electron detector operated in super-resolution counting mode with a binned pixel size of 1.088 Å. Each image was dose-fractionated to 40 frames with a total exposure time of 8 s with 0.2 s per frame. Dose rate was 6.76 e<sup>-</sup> Å<sup>-2</sup> s<sup>-1</sup>. The images were recorded using the automated acquisition program SerialEM<sup>49</sup>. Nominal defocus values varied from 1.2 to 2.4 μm.

**EM data processing.** Images were motion-corrected, summed, and 2 × 2 binned in Fourier space using MotionCor<sup>2</sup><sup>50</sup>. Defocus values were estimated using Gctf<sup>51</sup>. Particles from 100 micrographs were picked using Gautomatch (<http://www.mrc-lmb.cam.ac.uk/kzhang/Gautomatch/>) and subjected to an initial reference-free 2D classification using Relion<sup>52</sup>. Eight representative 2D class averages were selected as templates for automated particle picking for the entire data set using Gautomatch. The auto-picked particles were visually checked and false positives were removed. The particles were further cleaned up by several rounds of 2D classification using Relion. The CTF values of individual particles from selected 2D class averages were estimated using Gctf<sup>51</sup>. Initial reconstruction was obtained using cryoSPARC<sup>53</sup>. The particles were then classified into 5 classes using 3D classification function in Relion, with the initial reconstruction low-pass-filtered to 50 Å as reference model. Particles from each class were individually refined with C4 symmetry using Relion. Only two out of five reconstructions showed high-resolution features. There were no obvious conformational differences between the two best reconstructions. Therefore, particles from these two classes were combined and refined using Relion. Particles were further refined using the local refinement from Frealign with C4 symmetry applied<sup>54</sup>. The final resolutions reported in Extended Data Table 1 are based on the gold standard Fourier shell correlation (FSC) 0.143 criteria<sup>52</sup>. To calculate the FSC plot, a soft mask (3.26 Å extended from the reconstruction with an additional 3.26 Å cosine soft edge) was applied to the two half maps.

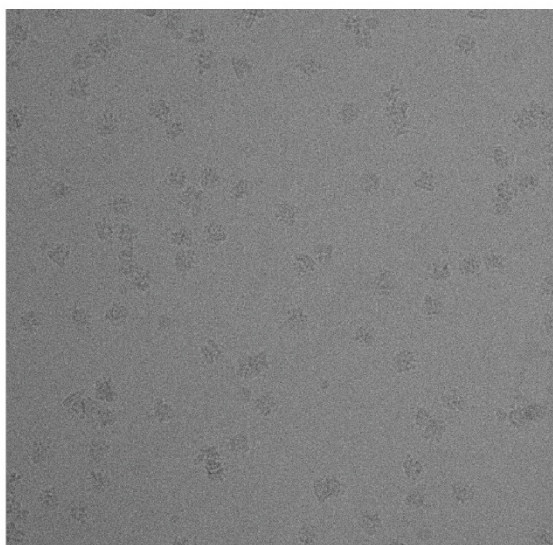
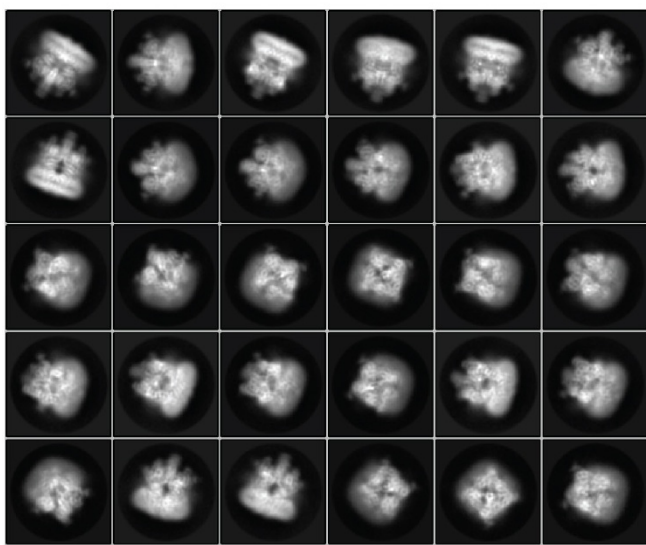
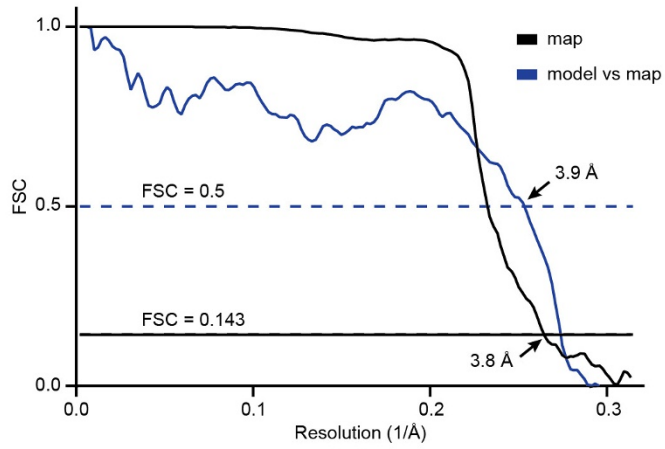
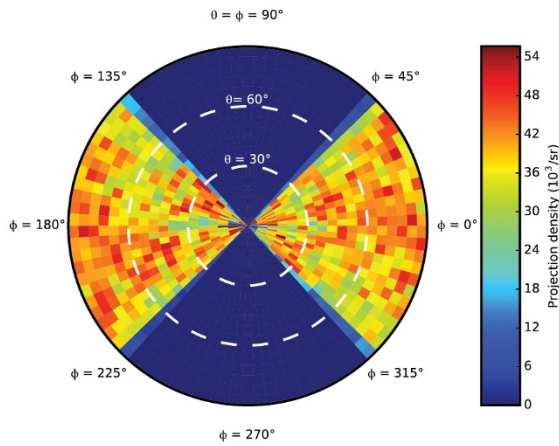
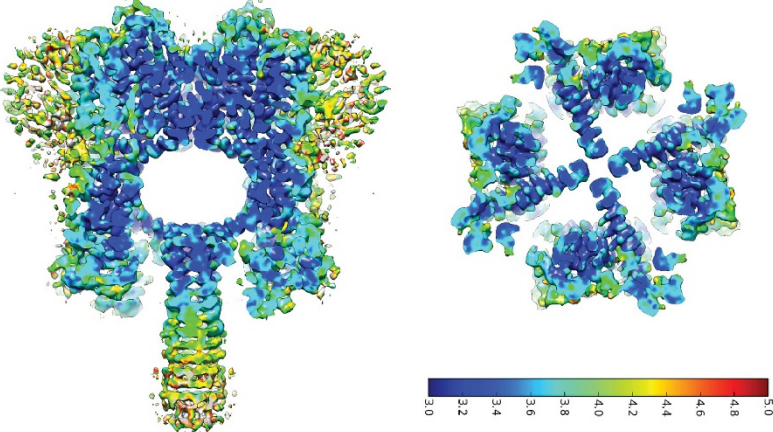
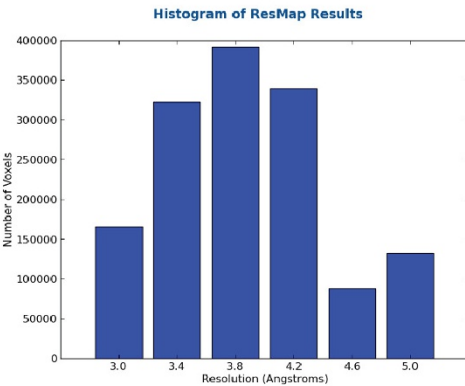
**Model building.** The TMD, TRP domain and MHR4 was built in COOT using the NOMPC structure as a guide<sup>28,55</sup>. For other cytosolic domains, α-helical features were first identified in the density map. *De novo* building and sequence assignment was mainly guided by bulky residues and secondary structure prediction (Extended Data Fig. 7). The TRPM4 structure mostly consists of α helices, which greatly assisted register assignment. Moreover, there is a GFP fusion protein

before the N terminus. The fact that the GFP, despite not being visible in the map (probably due to flexibility), cannot be buried inside of the protein provides a useful aid for determining the position of the N terminus. The densities for the last twenty amino acids in the C terminus (1174–1193) are not well defined in the sharpened map. These twenty amino acids are rigid-body fitted into an unsharpened map as an α helix according to secondary structure prediction. In the initial *de novo*-built model, the order and length of the secondary structure features, as well as the positions of bulky residues within each secondary structure feature are in good agreement with the prediction (Extended Data Fig. 7). The initial model was then subjected to molecular dynamics fitting<sup>56</sup> refinement, followed by real space refinement using Phenix.real\_space\_refine with secondary structure restraints. The refined model was further manually inspected and adjusted in COOT. The densities at both DVT sites are rhombohedron-shaped similar to a DVT molecule. Owing to limited resolution we tentatively placed DVT molecules into the two densities in a way such that the long axis of DVT molecule matches the long axis of the densities. For validation, FSC curves were calculated between the final model and EM map. The model to map correlation coefficient (0.792) was calculated using Phenix.map\_model\_cc(CC<sub>mask</sub>). The geometries of the atomic models were evaluated using MolProbity<sup>57</sup>. All figures were prepared using UCSF Chimera<sup>58</sup> and PyMol (Schrödinger)<sup>59</sup>.

**Electrophysiology.** HEK-293 cells were transfected using 293fectin kit (Thermo Fisher) according to the manufacturer's protocol. Cells were recorded 12–24 h post-transfection. Inside-out patches were pulled from transfected cells and recordings were performed using an Axopatch 1D amplifier (Molecular Devices) at room temperature. The holding potential was +60 mV or as otherwise indicated. The electrodes were filled with internal solution containing 150 mM NaCl, 10 mM HEPES, and 3 mM KCl, pH 7.4 (adjusted with NaOH). The bath solution was the same as the internal solution; a bath solution with 0.5 mM, 1 mM or 5 mM CaCl<sub>2</sub> added was used for channel activation. Solution change was done using either a two-barrel theta-glass pipette controlled by a Piezo bimorph or was done manually. Data were acquired at 20 kHz, filtered at 1 kHz, and analysed with Axograph software (<https://axograph.com/>). For alternating voltage jump experiments (100 mV to –100 mV, each voltage for 1 s) and current–voltage experiments (–140 mV to 140 mV with a step size of 20 mV and step length of 500 ms), TRPM4 currents were isolated by subtracting currents recorded without Ca<sup>2+</sup> from those recorded with Ca<sup>2+</sup>. DVT was made as described above, and the solution was used within 60 min of dissolving the powder in water.

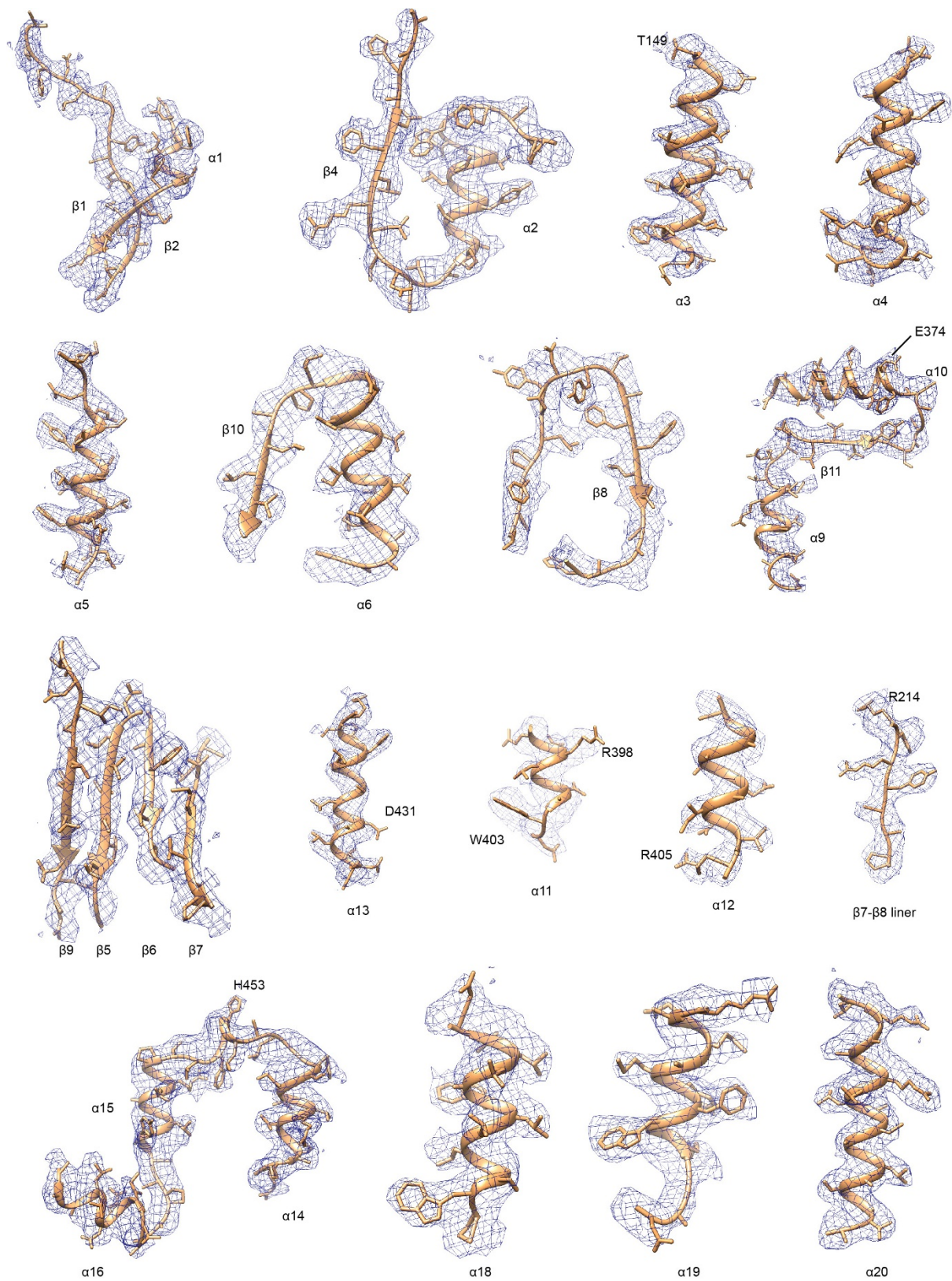
**Data Availability.** The cryo-EM density map and coordinates of TRPM4 have been deposited in the Electron Microscopy Data Bank (EMDB) accession number EMD-8871, and in the RCSB Protein Data Bank (PDB) accession code 5WP6.

46. Goehring, A. et al. Screening and large-scale expression of membrane proteins in mammalian cells for structural studies. *Nat. Protoc.* **9**, 2574–2585 (2014).
47. Varga, S., Csermely, P. & Martonosi, A. The binding of vanadium (V) oligoanions to sarcoplasmic reticulum. *Eur. J. Biochem.* **148**, 119–126 (1985).
48. Csanády, L. & Adam-Vizi, V. Antagonistic regulation of native Ca<sup>2+</sup>- and ATP-sensitive cation channels in brain capillaries by nucleotides and decavanadate. *J. Gen. Physiol.* **123**, 743–757 (2004).
49. Mastronarde, D. N. Automated electron microscope tomography using robust prediction of specimen movements. *J. Struct. Biol.* **152**, 36–51 (2005).
50. Zheng, S., Palovcak, E., Armache, J.-P., Cheng, Y. & Agard, D. Anisotropic correction of beam-induced motion for improved single-particle electron cryo-microscopy. *bioRxiv* (2016).
51. Zhang, K. Gctf: Real-time CTF determination and correction. *J. Struct. Biol.* **193**, 1–12 (2016).
52. Scheres, S. H. W. RELION: implementation of a Bayesian approach to cryo-EM structure determination. *J. Struct. Biol.* **180**, 519–530 (2012).
53. Punjani, A., Rubinstein, J. L., Fleet, D. J. & Brubaker, M. A. cryoSPARC: algorithms for rapid unsupervised cryo-EM structure determination. *Nat. Methods* **14**, 290–296 (2017).
54. Grigorieff, N. Frealign. *Methods Enzymol.* **579**, 191–226 (2016).
55. Emsley, P., Lohkamp, B., Scott, W. G. & Cowtan, K. Features and development of Coot. *Acta Crystallogr. D* **66**, 486–501 (2010).
56. Singhary, A. et al. Molecular dynamics-based refinement and validation for sub-5 Å cryo-electron microscopy maps. *eLife* **5**, e16105 (2016).
57. Chen, V. B. et al. MolProbity: all-atom structure validation for macromolecular crystallography. *Acta Crystallogr. D* **66**, 12–21 (2010).
58. Pettersen, E. F. et al. UCSF Chimera—a visualization system for exploratory research and analysis. *J. Comput. Chem.* **25**, 1605–1612 (2004).
59. DeLano, W. L. *The PyMOL Molecular Graphics System*; <http://www.pymol.org> (2002).

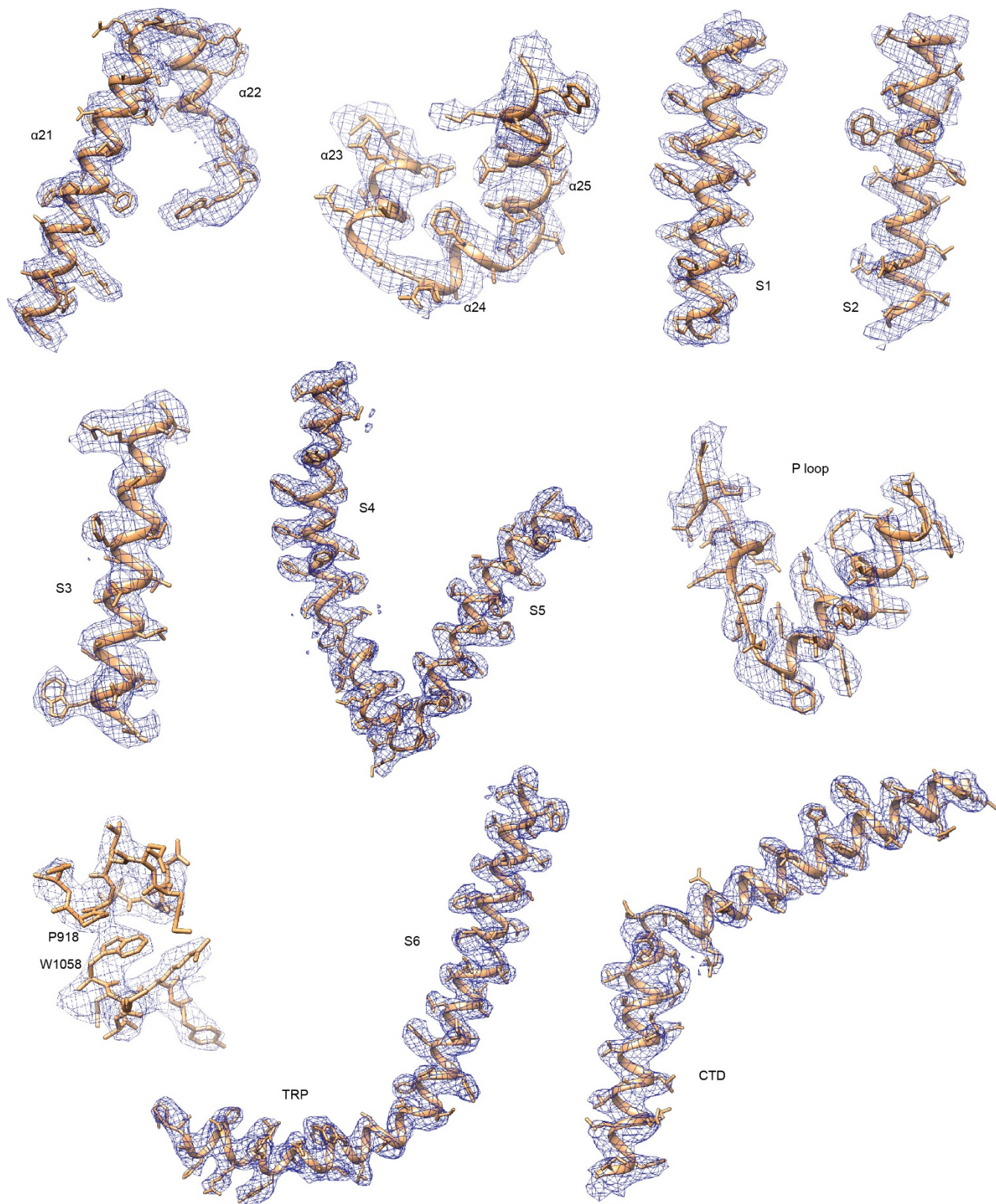
**a****b****c****d****e****f****g**

**Extended Data Figure 1 | Cryo-EM analysis of TRPM4 in complex with agonist calcium and the modulator DVT.** **a**, Representative electron micrograph. **b**, Selected two-dimensional class averages of the electron micrographs. **c**, The gold-standard Fourier shell correlation curves for the

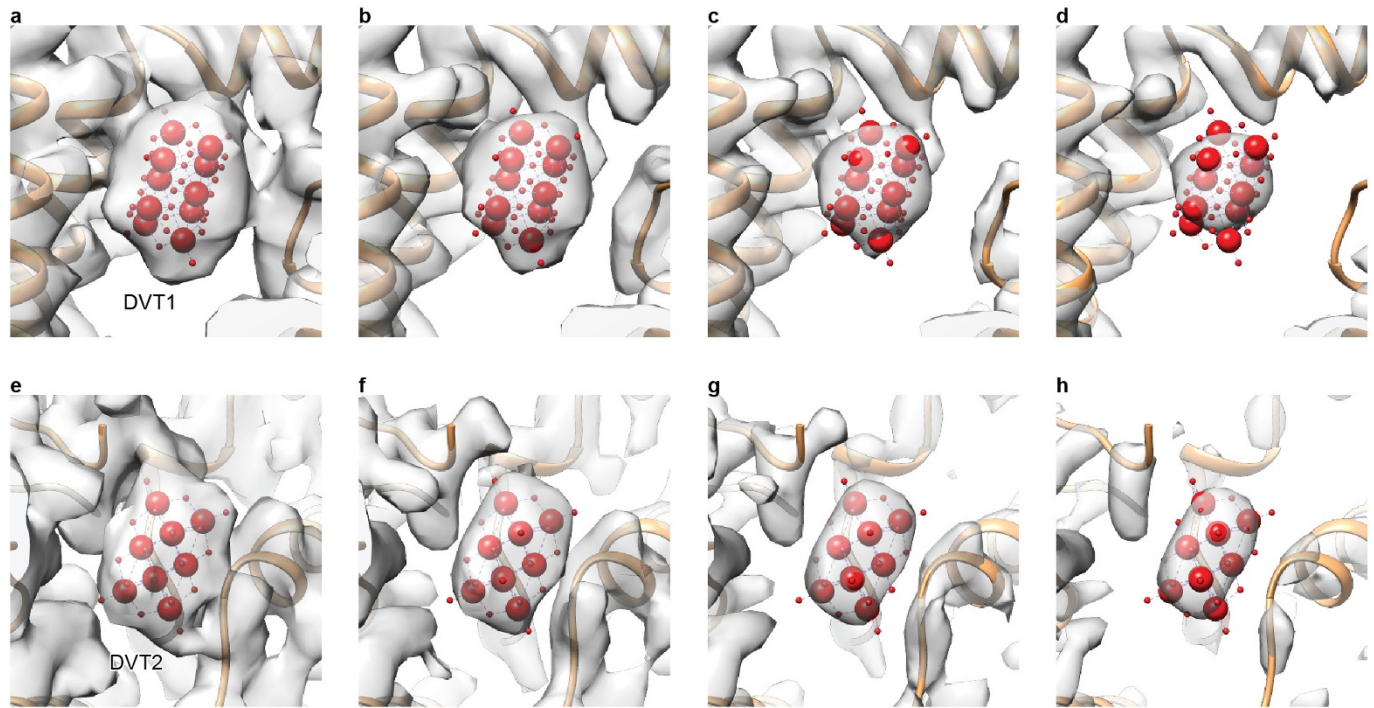
electron microscopy maps are shown in black and the FSC curves between the atomic model and the final EM map are shown in blue. **d**, Angular distribution of particles used for refinement. **e–g**, Local resolution estimation. The map is coloured according to local resolution estimation.



Extended Data Figure 2 | Representative densities of the reconstruction of TRPM4.

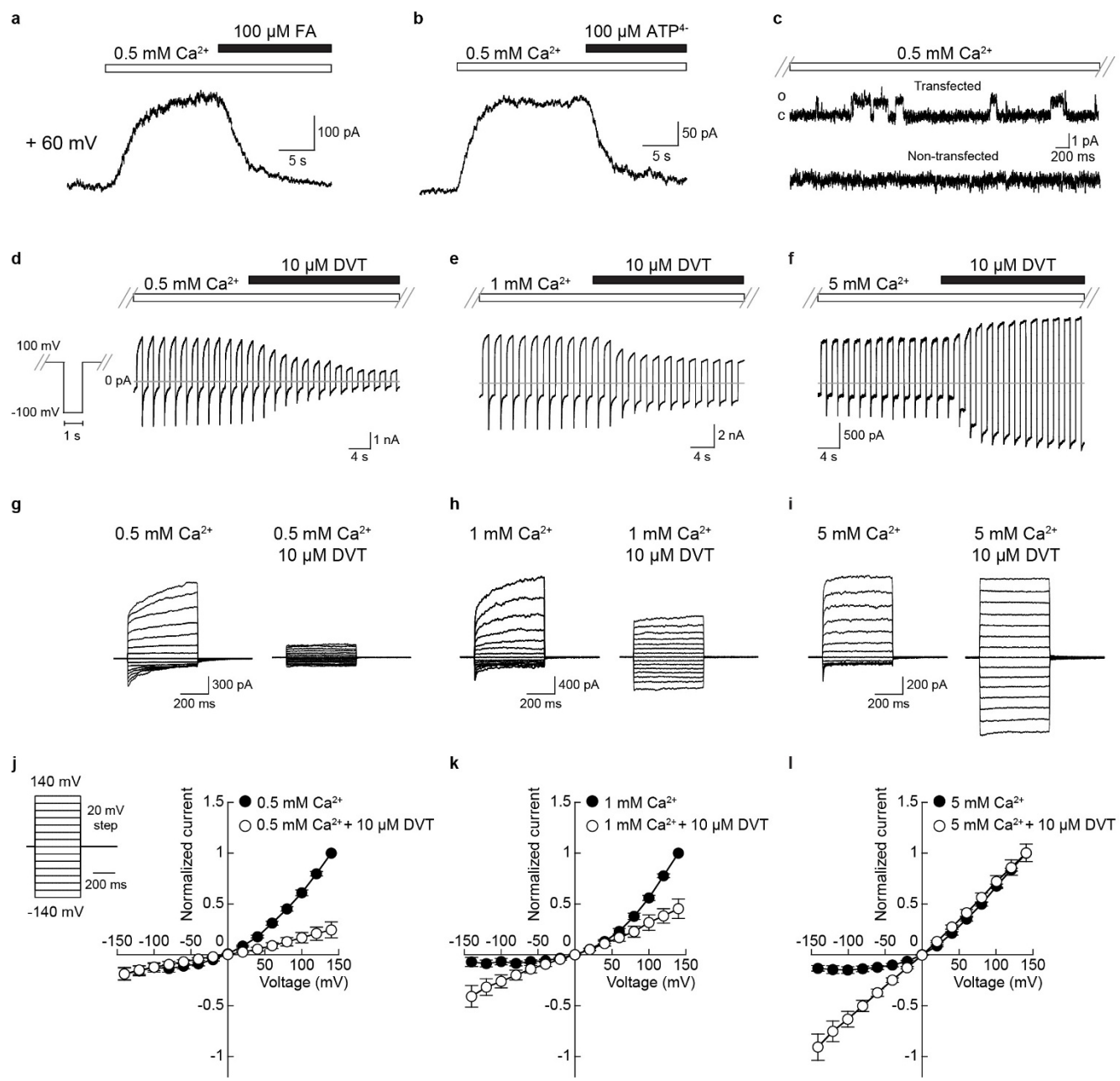


Extended Data Figure 3 | Representative densities of the reconstruction of TRPM4 (continued).



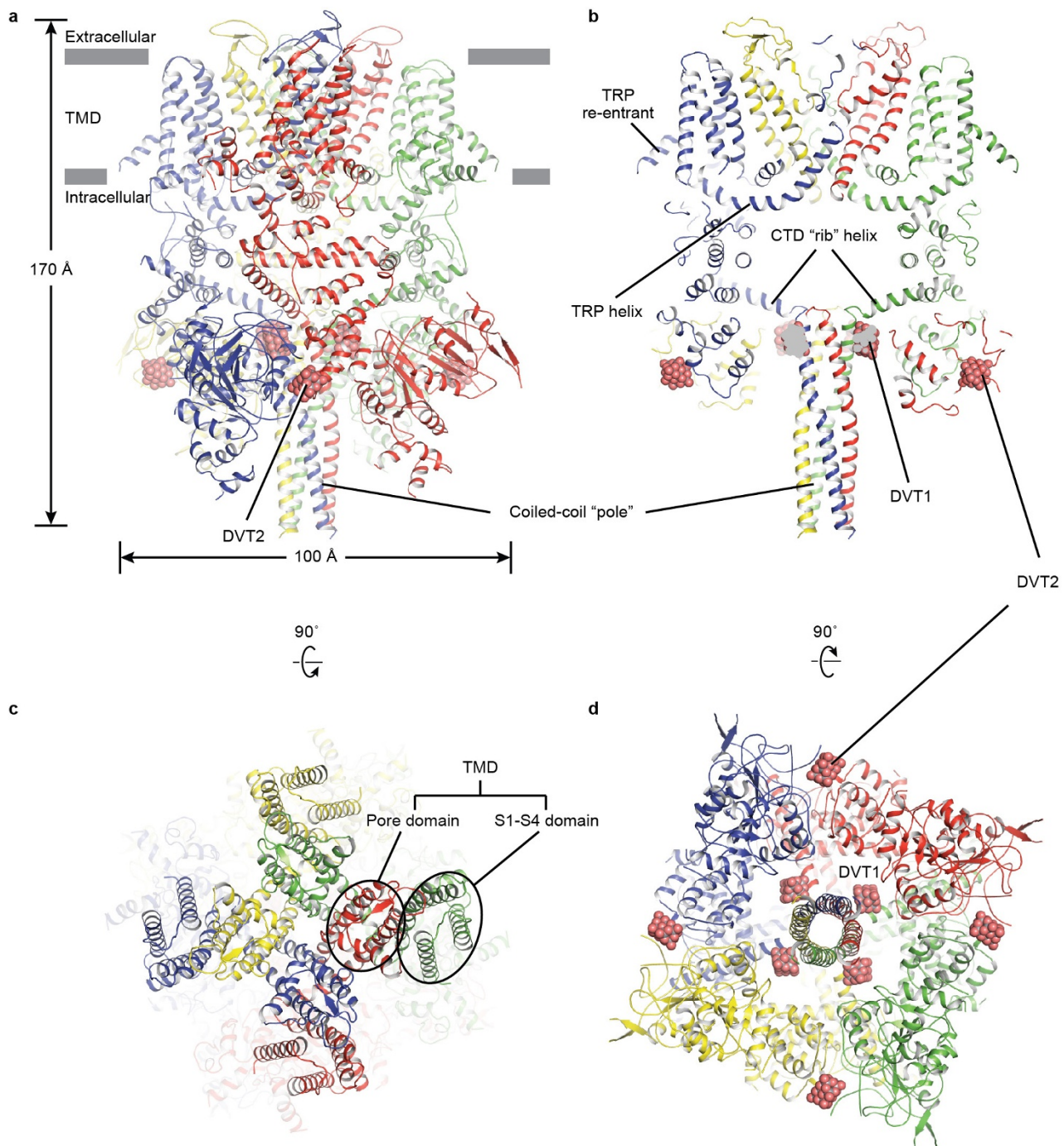
**Extended Data Figure 4 | Densities of DVT1, DVT2 and neighbouring protein.** a–d, DVT1. e–h, DVT2. Protein is shown in cartoon representation, whereas DVT molecules are shown in spheres and lines. The densities are contoured at different  $\sigma$  levels (from left to right, 0.03

(a, e), 0.04 (b, f), 0.05 (c, g) and 0.06 (d, h)), showing strong densities of DVT molecules and clear boundaries between DVT molecules and neighbouring protein.

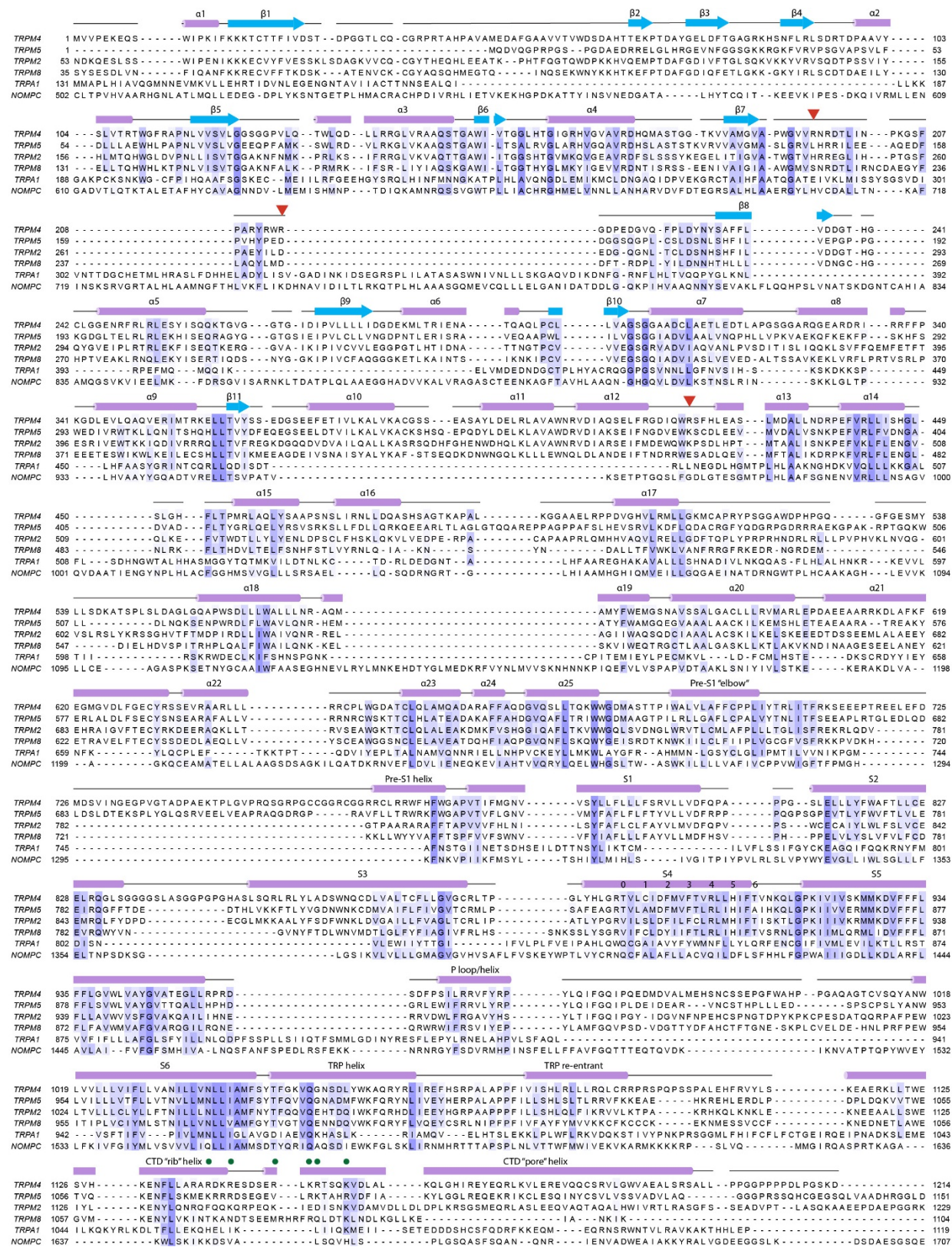


**Extended Data Figure 5 | Calcium activation and DVT modulation of TRPM4.** **a**, Application of  $0.5 \text{ mM } \text{Ca}^{2+}$  onto inside-out patches pulled from HEK-293 cells transfected with TRPM4 plasmid elicited currents at  $+60 \text{ mV}$ . Flufenamic acid (FA,  $100 \mu\text{M}$ ) blocked the  $\text{Ca}^{2+}$  induced current by  $98 \pm 6\%$  ( $n = 3$  cells). **b**,  $100 \mu\text{M } \text{ATP}^{4-}$  blocked  $\text{Ca}^{2+}$  induced current by  $81 \pm 11\%$  ( $n = 3$  cells). **c**, Top, an inside-out patch showing single channel activity when exposed to  $0.5 \text{ mM } \text{Ca}^{2+}$ . Single channel current had a mean amplitude of  $1.8 \text{ pA}$ , corresponding to a single channel conductance of  $30 \text{ pS}$ . Bottom, channel activities were not observed from non-transfected cells ( $n = 4$  cells). **d-f**, After application of  $0.5 \text{ mM}$  (**d**),  $1 \text{ mM}$  (**e**) or  $5 \text{ mM}$  (**f**)  $\text{CaCl}_2$ , alternating voltage commands were delivered ( $\pm 100 \text{ mV}, 1 \text{ s}$  pulses). Once the current amplitude at both voltages stabilized,  $10 \mu\text{M } \text{DVT}$  was co-applied with  $\text{CaCl}_2$ . At  $0.5 \text{ mM } \text{Ca}^{2+}$ ,  $10 \mu\text{M } \text{DVT}$  blocked  $\text{Ca}^{2+}$  induced currents by  $67 \pm 5\%$  ( $n = 4$  cells,  $P = 0.001$ ) at  $+100 \text{ mV}$  and did not change current amplitude at  $-100 \text{ mV}$  ( $n = 4$  cells,  $P = 0.148$ ). At  $1 \text{ mM } \text{Ca}^{2+}$ ,  $10 \mu\text{M } \text{DVT}$  blocked  $\text{Ca}^{2+}$  induced currents by  $56 \pm 14\%$  ( $n = 4$  cells,  $P = 0.013$ ) at  $+100 \text{ mV}$  while  $10 \mu\text{M } \text{DVT}$  potentiated the currents by  $322 \pm 83\%$  at  $-100 \text{ mV}$  ( $n = 4$  cells,  $P = 0.030$ ). At  $5 \text{ mM } \text{Ca}^{2+}$ ,  $10 \mu\text{M } \text{DVT}$  did not change current amplitude ( $n = 4$  cells,  $P = 0.517$ ) but potentiated  $\text{Ca}^{2+}$  induced currents at  $-100 \text{ mV}$  by  $520 \pm 147\%$  ( $n = 4$  cells,  $P = 0.035$ ). Two-sided  $t$ -tests were used for statistical comparisons. Observations of the inhibitory effect of DVT

at  $0.5 \text{ mM } \text{Ca}^{2+}$  is more pronounced compared to previously reported data<sup>21</sup>, where the authors only occasionally saw inhibitory effect of DVT at positive potentials, and the extent of inhibition was less pronounced. The reason for this discrepancy is not clear; we suspect differences in construct, solution composition, solution pH, cell line, transfection methods, other variations in experimental protocols or combinations of these factors. Although the effects of DVT on current amplitude varied with calcium concentration,  $10 \mu\text{M } \text{DVT}$  linearized the current–voltage relationship in all three calcium concentrations (see **g–l**). **g–i**,  $500 \text{ ms}$  voltage pulses ranging from  $-140 \text{ mV}$  to  $140 \text{ mV}$  from a holding potential of  $0 \text{ mV}$  ( $20 \text{ mV}$  step size) were used to obtain the current–voltage relationship. Currents recorded in the presence of  $0.5 \text{ mM}$  (**g**, left),  $1 \text{ mM}$  (**h**, left) or  $5 \text{ mM}$  (**i**, left)  $\text{Ca}^{2+}$ . Currents recorded in the presence of  $0.5 \text{ mM}$  (**g**, right),  $1 \text{ mM}$  (**h**, right) or  $5 \text{ mM}$  (**i**, right)  $\text{Ca}^{2+}$  with  $10 \mu\text{M } \text{DVT}$  from the same patch. **j–l**, Currents recorded with  $\text{Ca}^{2+}$  and  $\text{Ca}^{2+}$  and DVT ( $\text{Ca}^{2+}$  concentrations as in **g–i**) at different voltages, data are normalized to the amplitude of current recorded with  $\text{Ca}^{2+}$  at  $140 \text{ mV}$ . **g–l**, Data are mean  $\pm$  s.e.m. from four (**h**, **i**, **k**, **l**) or five (**g**, **j**) cells, experiments repeated three times for each cell. Leak currents were obtained by running the same voltage command when no calcium was applied and were subtracted from the currents recorded in  $\text{Ca}^{2+}$  for all experiments in **d–l**.

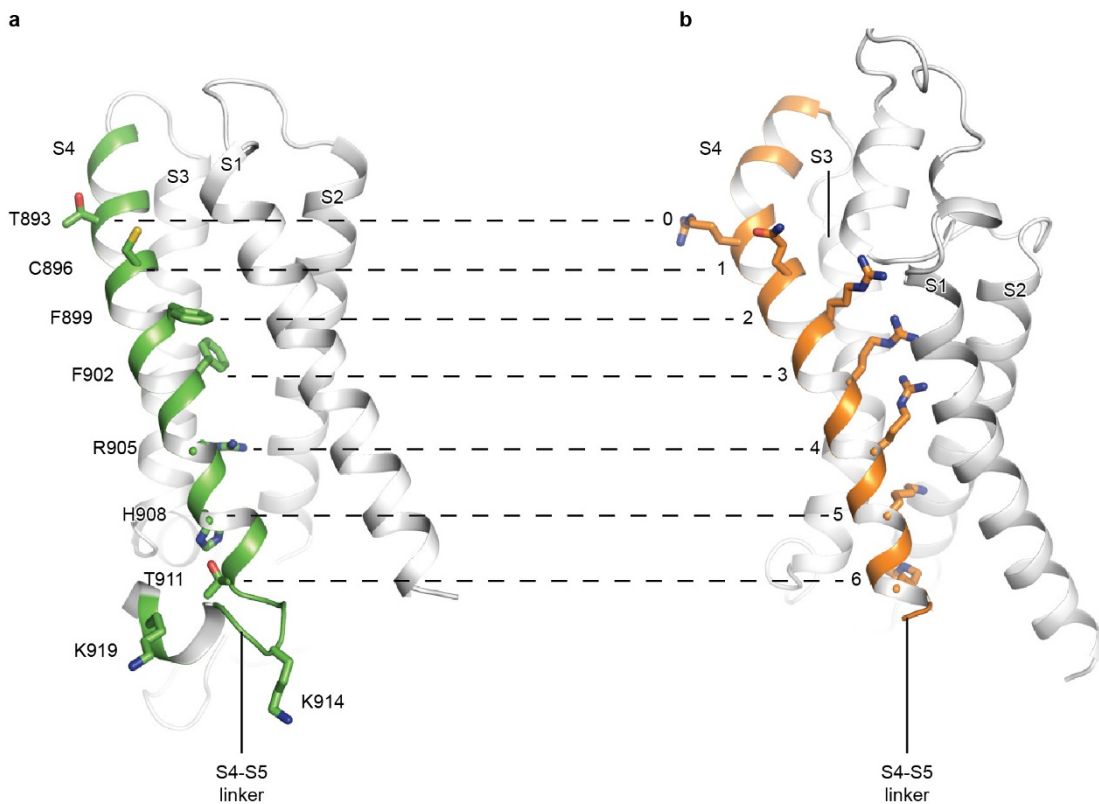


**Extended Data Figure 6 | Structure of TRPM4.** **a**, TRPM4 tetramer viewed parallel to the membrane. **b–d**, Slice views of **a**, viewed from parallel to the membrane (**b**), from the extracellular side of the membrane (**c**), or from the cytosolic side (**d**). The four subunits are in blue, pink, green and yellow.



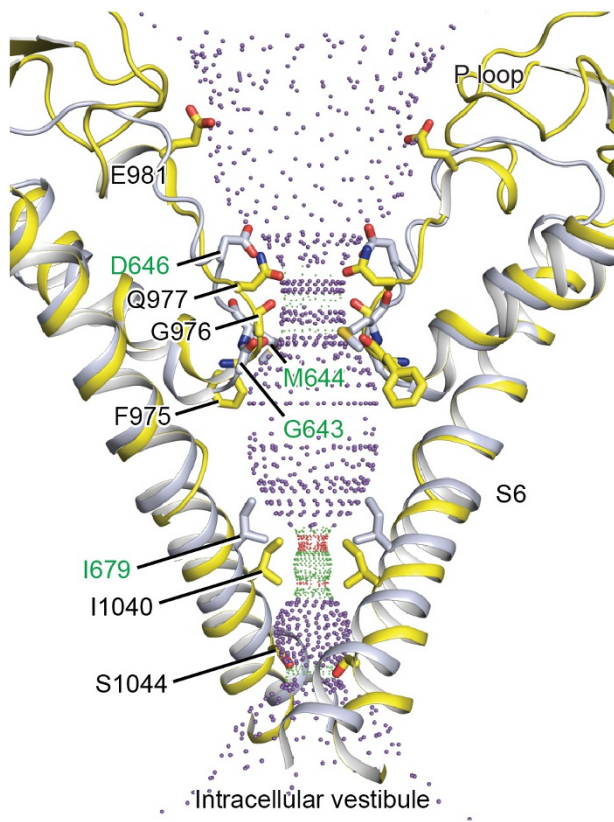
**Extended Data Figure 7 | Secondary structure prediction of human TRPM4 and sequence alignment of TRPM4, TRPM5, TRPM2, TRPM8, TRPA1 and NOMPC.** The NOMPC is from *Drosophila*, whereas all the other proteins are human. The secondary structure prediction of TRPM4 was done using the JPred online server. The sequences were aligned using the Clustal Omega program on the UniProt website and coloured using

BLOSUM62 score by conservation. Residues that coordinate DVT1 or DVT2 in TRPM4 are marked with filled circles or triangles, respectively. Residues that correspond to R0, Q1, R2, R3, R4, K5 and R6 in the S4 of KyChim (PDB accession number 2R9R, Extended Data Fig. 8) are marked with 0, 1, 2, 3, 4, 5 and 6, respectively.



**Extended Data Figure 8 | Comparison of the voltage sensor domain (S1–S4) in TRPM4 and in Kvchim.** **a, b,** The S4 and S4–S5 linker in TRPM4 (**a**) or Kvchim (**b**) are in green or orange, respectively. The residues at positions R0, Q1, R2, R3, R4, R5 and R6 in Kvchim, and the

corresponding residues in TRPM4 are shown as sticks. The two positively charged residues (K914 and K919) in S4–S5 linker of TRPM4 are also shown as sticks.



**Extended Data Figure 9 | Comparison of the pore in TRPM4 (yellow) and in TRPV1 (grey).** The P loop and S6 of two subunits are shown in cartoon representation and the side chains of restriction residues are shown as sticks. Restriction residues in TRPM4 or TRPV1 are in black or green, respectively. Purple, green, and red spheres define radii of  $>2.3$ ,  $1.2\text{--}2.3$ , and  $<1.2\text{\AA}$ , respectively.

Extended Data Table 1 | Statistics of EM data processing and model refinement

**Data collection/processing**

Microscope	Titan Krios (FEI)
Voltage (kV)	300
Defocus range ( $\mu\text{M}$ )	1.2 – 2.4
Exposure time (s)	8
Dose rate ( $e^-/\text{\AA}^2/\text{s}$ )	6.76
Number of frames	40
Pixel size ( $\text{\AA}$ )	1.088
Particles refined	121906
Resolution ( $\text{\AA}$ )	3.8
FSC threshold	0.143
Resolution range ( $\text{\AA}$ )	487 – 3.8

**Model statistics**

Number of atoms	29044
Protein	28740
Ligand	304
r.m.s. deviations	
Bond length ( $\text{\AA}$ )	0.09
Bond angle ( $^\circ$ )	1.27
Ramachandran plot	
Favored (%)	93.33
Allowed (%)	6.67
Disallowed (%)	0
Rotamer outlier (%)	0.3
Clashscore	3.0
MolProbity score	1.5

# Life Sciences Reporting Summary

Nature Research wishes to improve the reproducibility of the work that we publish. This form is intended for publication with all accepted life science papers and provides structure for consistency and transparency in reporting. Every life science submission will use this form; some list items might not apply to an individual manuscript, but all fields must be completed for clarity.

For further information on the points included in this form, see [Reporting Life Sciences Research](#). For further information on Nature Research policies, including our [data availability policy](#), see [Authors & Referees](#) and the [Editorial Policy Checklist](#).

## ► Experimental design

### 1. Sample size

Describe how sample size was determined.

All the electrophysiological experiments are repeated at least three times using different cells. The sample size is determined based on the consistency of the recordings.

### 2. Data exclusions

Describe any data exclusions.

Transfected cells that did not show currents upon application of calcium are excluded.

### 3. Replication

Describe whether the experimental findings were reliably reproduced.

All the electrophysiological experiments are repeated reliably for each cell.

### 4. Randomization

Describe how samples/organisms/participants were allocated into experimental groups.

For electrophysiological experiments, cells with GFP fluorescence (proteins were GFP-tagged) were randomly selected.

### 5. Blinding

Describe whether the investigators were blinded to group allocation during data collection and/or analysis.

The investigators were blinded to group allocation during data collection and analysis.

Note: all studies involving animals and/or human research participants must disclose whether blinding and randomization were used.

### 6. Statistical parameters

For all figures and tables that use statistical methods, confirm that the following items are present in relevant figure legends (or in the Methods section if additional space is needed).

n/a Confirmed

- The exact sample size (*n*) for each experimental group/condition, given as a discrete number and unit of measurement (animals, litters, cultures, etc.)
- A description of how samples were collected, noting whether measurements were taken from distinct samples or whether the same sample was measured repeatedly
- A statement indicating how many times each experiment was replicated
- The statistical test(s) used and whether they are one- or two-sided (note: only common tests should be described solely by name; more complex techniques should be described in the Methods section)
- A description of any assumptions or corrections, such as an adjustment for multiple comparisons
- The test results (e.g. *P* values) given as exact values whenever possible and with confidence intervals noted
- A clear description of statistics including central tendency (e.g. median, mean) and variation (e.g. standard deviation, interquartile range)
- Clearly defined error bars

See the web collection on [statistics for biologists](#) for further resources and guidance.

## ► Software

Policy information about [availability of computer code](#)

### 7. Software

Describe the software used to analyze the data in this study.

gctf, gautomatch, relion, frealign, cryosparc, coot, pymol, MotionCor2, Phenix.real\_space\_refine, Phenix.map\_model\_cc, MolProbity, UCSF Chimera, Axograph software.

For manuscripts utilizing custom algorithms or software that are central to the paper but not yet described in the published literature, software must be made available to editors and reviewers upon request. We strongly encourage code deposition in a community repository (e.g. GitHub). *Nature Methods* guidance for [providing algorithms and software for publication](#) provides further information on this topic.

## ► Materials and reagents

Policy information about [availability of materials](#)

### 8. Materials availability

Indicate whether there are restrictions on availability of unique materials or if these materials are only available for distribution by a for-profit company.

all unique materials are readily available from the authors

### 9. Antibodies

Describe the antibodies used and how they were validated for use in the system under study (i.e. assay and species).

n/a

### 10. Eukaryotic cell lines

a. State the source of each eukaryotic cell line used.

Sf9 cells and HEK293 GnTl– cells are purchased from ATCC

b. Describe the method of cell line authentication used.

Sf9 cells and HEK293 GnTl– cells are not authenticated.

c. Report whether the cell lines were tested for mycoplasma contamination.

Sf9 and HEK293 GnTl– cells were not tested for mycoplasma contamination

d. If any of the cell lines used are listed in the database of commonly misidentified cell lines maintained by [ICLAC](#), provide a scientific rationale for their use.

no commonly misidentified cell lines were used.

## ► Animals and human research participants

Policy information about [studies involving animals](#); when reporting animal research, follow the [ARRIVE guidelines](#)

### 11. Description of research animals

Provide details on animals and/or animal-derived materials used in the study.

n/a

Policy information about [studies involving human research participants](#)

### 12. Description of human research participants

Describe the covariate-relevant population characteristics of the human research participants.

n/a